



Title	Self-assembly of MoO <sub>3</sub> needles in gas current for cubic formation pathway
Author(s)	Ishizuka, Shinnosuke; Kimura, Yuki; Yokoi, Satoki; Yamazaki, Tomoya; Sato, Rikako; Hama, Tetsuya
Citation	Nanoscale, 9(28), 10109-10116 <a href="https://doi.org/10.1039/c7nr02613g">https://doi.org/10.1039/c7nr02613g</a>
Issue Date	2017-06-20
Doc URL	<a href="http://hdl.handle.net/2115/70788">http://hdl.handle.net/2115/70788</a>
Type	article (author version)
Additional Information	There are other files related to this item in HUSCAP. Check the above URL.
File Information	Ishizuka_MoO <sub>3</sub> _Nanoscale_HUSCAP.pdf



[Instructions for use](#)

## Self-Assembly of MoO<sub>3</sub> Needles in Gas Current for Cubic Formation Pathway

Shinnosuke Ishizuka<sup>a</sup>, Yuki Kimura<sup>a\*</sup>, Satoki Yokoi<sup>b</sup>, Tomoya Yamazaki<sup>a</sup>, Rikako Sato<sup>a</sup> and Tetsuya Hama<sup>a</sup>

Received 00th January 20xx,  
Accepted 00th January 20xx

DOI: 10.1039/x0xx00000x

www.rsc.org/

Nucleation and subsequent rapid growth are enigmatic due to the unrevealed pathways. Despite the relatively simpler mechanism than nucleation and growth in solution, that in vapor has received little attentions. The largest hindrance to unveiling this process may be observing the rapid and mesoscopic-scale phenomena. To overcome this hindrance, we combine an experimental approach with in-situ spatial scanning Fourier-transform infrared spectroscopy, which reveals the nucleating and growing nanoparticles in vapor. The nanoparticles are then collected at different evolutionary stages and analyzed by ex-situ transmission electron microscopy (TEM). Needle-shaped molybdenum oxide (MoO<sub>3</sub>) nanoparticles were formed within ~0.1 s after homogeneous nucleation from a highly supersaturated vapor. Over one second, the needle particles gradually evolved into a cubic shape by fusion in a crystallographically favored orientation in a free-flying state in vapor. The similar sizes of the elongated axes of the needle and cubic structures suggest an additional growth stage, in which the needle particles become the growth units of the cubic particles. The morphology of a final crystal should reflect the formation environment of the particle because growing crystals are sensitive to the formation conditions such as temperature, concentration, and impurities. Although nucleation under very high supersaturation induces anisotropic growth of the needle particles, this information of the initial nucleation environment is lost in the final cubic crystal. These findings enrich our understanding of pathways in the nucleation and growth of nanoparticles and provide new insights into the growth stages driven by oriented attachment.

### 1 Introduction

2 Nucleation critically determines the characters (such  
3 crystalline size, shape, polymorphism, and crystallinity) of  
4 inorganic,<sup>1–8</sup> organic,<sup>9–11</sup> proteinaceous,<sup>12,13</sup> and colloidal<sup>14,15</sup>  
5 materials. In an ideal system, a crystal grows continuously  
6 toward its final form by sequential incorporation of growth  
7 units.  
8 In the last decade, in-situ observations have revealed  
9 unexpected nucleation pathways, especially in solution  
10 systems. These observations have overridden the previous  
11 simple view that nucleation proceeds by monomer-by-  
12 monomer incorporation of basic units. Before the stable  
13 crystal is formed, intermediates such as polymorphs,  
14 amorphous solid particles,<sup>3</sup> liquid droplets,<sup>6,7,12,13</sup> clusters with  
15 characteristic structures,<sup>4,11</sup> and crystals with different  
16 chemical compositions from the final crystal<sup>2</sup> precipitate out  
17 metastable phases. The formation sequence sometimes

18 follows Ostwald's step rule, in which the metastable  
19 intermediates precipitate due to lower surface energies than  
20 the stable phase.<sup>16</sup> This process is complicated by the  
21 characteristics of solvent molecules. To approach a kink site  
22 and thereby join the crystal, a growth unit in water must  
23 dehydrate the hydrated layer that surrounds the material.  
24 Dehydration process plays key roles at the early stage of  
25 nucleation and growth in solution.<sup>17,18</sup>

26 In contrast to complex nucleation from solution, nucleation  
27 of inorganic particles from a vapor is surface free, so we expect  
28 that the result to be comparable to the nucleation theory.  
29 Some experimental studies have attempted to unveil the  
30 nucleation process. For instance, after thermal evaporation at  
31 extremely high supersaturation, metal and metal oxides  
32 nucleate homogeneously in the cooling gas.<sup>19–21</sup> According to  
33 nucleation theory, the critical nuclei in manganese nucleation  
34 should be several atom/molecules in size, and their surface  
35 free energy should be 30% larger than that of the  
36 corresponding bulk.<sup>20</sup>

37 Unexpected pathways in the post-nucleation growth  
38 processes have also been proposed. Inter-particle coarsening  
39 is thought to determine the resulting characteristics of crystals  
40 in some solution systems.<sup>22</sup> When coarsening happens  
41 selectively between crystallographically equivalent planes, it is  
42 known as oriented attachment growth.<sup>e.g.,2,23–27</sup> For many  
43 years, the fusion of two nanoparticles and agglutination by

<sup>a</sup>Institute of Low Temperature Science, Hokkaido University, Hokkaido Sapporo 060-0819, Japan

<sup>b</sup>Department of Chemical Engineering, Graduate School of Engineering, Tohoku University, 6-6-07 Aoba, Aramaki, Aoba-ku, Sendai, Miyagi 980-8579, Japan

†Electronic Supplementary Information (ESI) available: Detailed description of the procedure of the collision simulation and supplementary figures of the experiment, IR spectra, TEM images and size distribution of the particles are available. See DOI: 10.1039/x0xx00000x

44 surface melting has been known to dominate the growth  
 45 process in vapor phase. These previous studies show that  
 46 nucleation and growth pathways are not simple processes  
 47 such as continuous incorporation of monomer molecules,  
 48 are universally more diverse than hitherto predicted.<sup>26,27</sup>  
 49 Here we experimentally investigate vapor phase nucleation  
 50 and subsequent growth of nanoparticles. Our proposed  
 51 approach captures the early stages of crystallization using  
 52 *situ* spatial scanning spectroscopy by a transmittance Fourier  
 53 transform infrared (FT-IR) spectrometer. The in-situ IR data  
 54 (which reflect the chemical compositions, phases, and shapes  
 55 of the just-nucleated nanoparticles in the free-flying state)  
 56 complemented by TEM observations of the collected products  
 57 Applied in vapor phase nucleation, this technique  
 58 demonstrates that morphological evolution of just-nucleated  
 59 MoO<sub>3</sub> nanoparticles is induced by inter-particle coarsening  
 60 crystallographically equivalent planes during frequent  
 61 collisions in the gas current.

## 62 Experimental section

63 Nucleation and subsequent growth experiments of MoO<sub>3</sub>  
 64 nanoparticles in vapor phase were performed in a stainless-  
 65 steel chamber combined with a FT-IR spectrometer (JASCO  
 66 VIR200), as described in our previous study.<sup>28</sup> The  
 67 experimental apparatus for forming nanoparticles in the gas  
 68 current is schematized in Figure S1a. The thallium bromoiodide  
 69 (KRS5) viewports provide an optical path for the FT-IR analysis.  
 70 KRS5 exhibits high transmittance in the 10000–250 cm<sup>-1</sup> range.  
 71 The transmitted IR light was sensed by a detector unit  
 72 comprising an aperture, an IR filter (LP-8335, IR System Co.,  
 73 Ltd., Tokyo, Japan), a parabolic mirror, and an HgCdTe (MCT)  
 74 photo-conductive detector (P5274-01, Hamamatsu Co.,  
 75 Shizuoka, Japan). The viewports were fixed to a U-shaped  
 76 bench on which the FT-IR and detector unit were set at either  
 77 side of the chamber. The chamber and viewports were  
 78 connected by flexibly extendable bellows. In addition, the  
 79 bench was interlocked to withstand a load motor unit  
 80 (LAS4F40MW-1, Oriental Motor Co., Tokyo, Japan). In this  
 81 configuration, we could acquire the transmittance FT-IR  
 82 spectra at different heights from the evaporation source in a  
 83 single experiment. The measurable region (65 mm along the  
 84 vertical axis) exceeded the inner diameter of the windows (30  
 85 mm). The bench height was measured by a laser measurement  
 86 sensor (CD22, OPTEX FA Co., Kyoto, Japan). The chamber was  
 87 connected to a turbo-molecular pump (50 L/s). After  
 88 evacuating the chamber to below  $1.0 \times 10^{-4}$  Pa, the gate valve  
 89 was closed and high-purity O<sub>2</sub> (99.9%) and He (99.9999%) were  
 90 injected. The pressure was first to  $4.0 \times 10^2$  Pa with O<sub>2</sub> gas,  
 91 then increased to  $5.0 \times 10^3$  Pa with He gas. The gas pressure  
 92 was measured by a crystal ion gauge (M-601GC, ANELVA Co.,  
 93 Kanagawa, Japan) at  $<10^{-1}$  Pa, and by a piezoresistive pressure  
 94 sensor (Pressure sensor 680, Huba Control, Switzerland) at  
 95 Pa.  
 96 The evaporation source was a Mo wire ( $\phi = 1$  mm, length = 75  
 97 mm, purity 99.95%). The wire was connected to Cu electrodes  
 98 for rapid electrical-resistance heating. At the starting position

in Experiment A and B, the optical axis of the FT-IR was  
 centered at 10 mm beneath and 7.5 mm above the  
 evaporation source, respectively. The temperature of the  
 evaporation source was monitored during the experiments by  
 a radiation thermometer ( $\lambda = 0.8$ – $1.6$   $\mu\text{m}$ ; FTZ2, Japan Sensor  
 Co., Tokyo, Japan). In the temperature calculation, the  
 emissivity of the Mo wire surface was assumed constant at 0.3.  
 However, because the emissivity changes by surface oxidation  
 of the Mo wire, the absolute temperature obtained in this  
 study may depend on the oxygen vapor pressure. The  
 evaporation source was rapidly heated to  $\sim 1900$  K by applying  
 an AC voltage to the electrodes, then maintained at this  
 temperature throughout each experiment. Once the  
 temperature had stabilized, the bench was moved toward the  
 vertical axis at  $10 \text{ mm s}^{-1}$ , until the optical path reached 10  
 mm and 67.5 mm above the evaporation source in Experiment  
 A and B, respectively. The bench was then returned to its  
 starting position at  $10 \text{ mm s}^{-1}$ . Smoke formation was  
 confirmed by a CMOS camera (MS-M33WT3, Mosquell Co.,  
 Ltd., Tokyo, Japan) as shown in Figure S2. When the U-shaped  
 bench began to move, the convection has become stationary,  
 as confirmed by the shape of the smoke. Several seconds after  
 the bench reached its starting position, the AC voltage was  
 turned off. The changes in temperature of the evaporation  
 source, pressure in the chamber and relative distance between  
 the optical axis and the evaporation source were recorded,  
 and the results are plotted in Figure S3 for the Experiment B.

Surface oxidation on the Mo wire results in MoO<sub>3</sub> formation.  
 As MoO<sub>3</sub> has higher vapor pressure than Mo metal, the  
 oxidized MoO<sub>3</sub> was simultaneously evaporated as molecules  
 from the evaporation source. The gas flowed upward under  
 thermal convection generated by the evaporation source itself,  
 inducing the homogeneous nucleation of nanoparticles. The  
 nucleation was visible as a smoke. By setting the optical path  
 of the FT-IR just above the evaporation source, we could  
 measure the IR spectra of the nascent condensates in the free-  
 flying state. The aperture diameter was adjusted to improve  
 the spatial resolution at a suitable IR signal intensity. At an  
 aperture diameter of  $8 \pm 1$  mm, the beam diameter at the  
 center of the optical axis (where the nanoparticles were  
 nucleated) was calculated as  $4.5 \pm 0.6$  mm. The measurement  
 region was a column of width 5 mm (Figure S1b). The time  
 evolution of the IR spectra was obtained at 24 spectra/s. The  
 background spectra were obtained at each height from the  
 evaporation source, following the procedure just before the  
 experiment. The signal spectra in each 5-mm region were  
 averaged, and the absorbance spectra were then obtained  
 from 7.5 mm to 67.5 mm above the evaporation source. To  
 confirm the consistency of the region-dependent IR spectra in  
 the smoke, the spatial scan spectra were obtained in both  
 outward and homeward directions.

Some ascending nanoparticles were attached to stainless-  
 steel collecting sheets; one fixed at 10 mm beside the  
 evaporation source, the other fixed at more than 250 mm  
 above the evaporation source. The collected particles were  
 picked up on a standard Cu grid sweated with ethanol and  
 dried for 1 minute. The particles were observed by TEM (JEM-

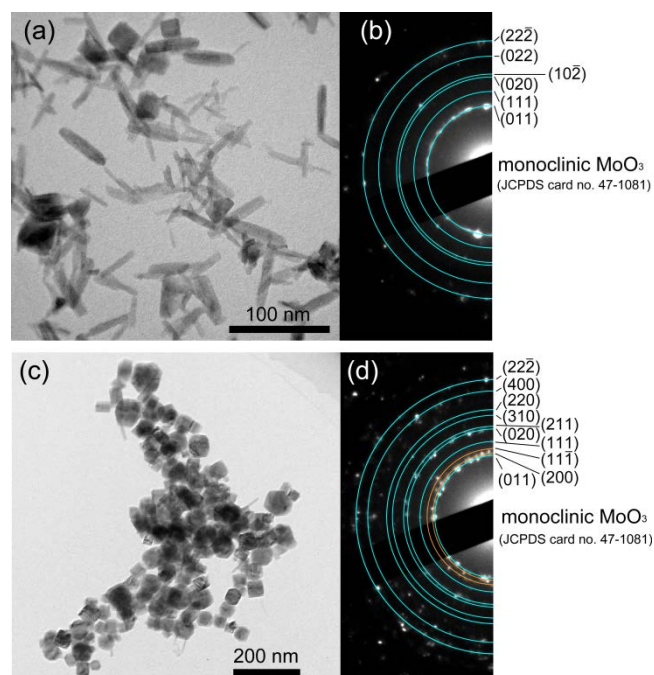


Figure 1. Typical TEM images of the synthesized nanoparticles collected (a) at the height of the evaporation source on the side collector set beside and (c) at the roof collector. (b), (d) electron diffraction (ED) patterns corresponding to (a) and (c), respectively.

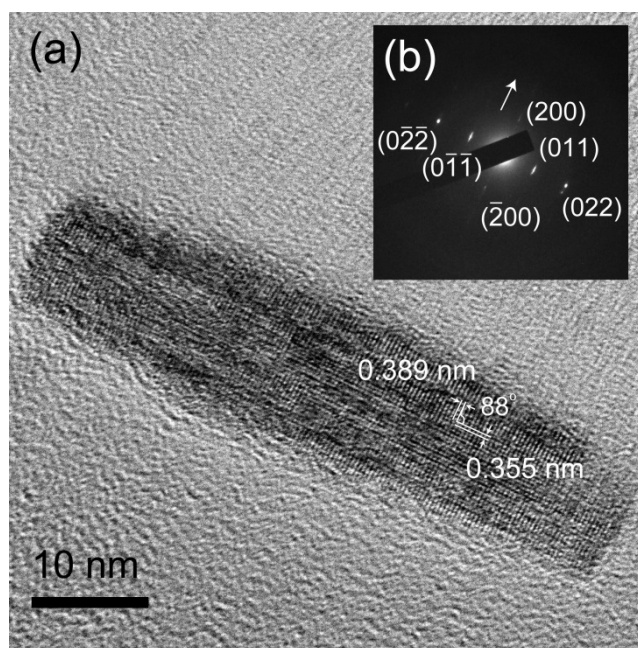


Figure 2. High resolution image of a typical needle shaped particle and (b) its corresponding ED pattern. Streaks along [200] are indicated by the white allow.

156 2100F, JEOL Co., Japan) at an acceleration voltage of 200 kV.  
 157 The remaining particles on the collecting sheet were agitated  
 158 with KBr powder and formed into 10 mm-diameter pellets  
 159 under a pressure of  $8 \times 10^4$  N for subsequent FT-IR  
 160 measurements.

## 161 Results

162 Molybdenum (Mo) wire was heated in a regulated gas  
 163 mixture of reactant oxygen ( $P_{O_2} = 4.0 \times 10^2$  Pa) and buffer  
 164 helium ( $P_{He} = 4.6 \times 10^3$  Pa). The oxidation and subsequent  
 165 evaporation of  $MoO_3$  and the nucleation of nanoparticles were  
 166 confirmed as visible smoke. Convection carries the evaporated  
 167  $MoO_3$  gas around the evaporation source. Consequently, the  
 168 gas concentration is highest at the bottom of the evaporation  
 169 source and nucleation is induced at several millimeters  
 170 beneath the Mo wire. High  $O_2$  partial pressure induces efficient  
 171 oxidation and evaporation of Mo source. In addition, high total  
 172 pressure induces frequent collision between the just-nucleated  
 173 nanoparticles in gas current. These leads increase in size of  
 174 resulting materials and reduce the time scale for shape  
 175 evolution.<sup>29</sup> We selected relatively low  $O_2$  partial pressure and  
 176 total pressure conditions (less frequent collision condition) in  
 177 order to clarify the particle formation sequences in the spatial  
 178 resolution of our experimental system. Nucleated  $MoO_3$   
 179 nanoparticles appear floating in the ascending gas current  
 180 generated by the hot evaporation source. The  $MoO_3$   
 181 nanoparticles are then cooled in the convection from  
 182 nucleation temperature (typically around 1000 K) to room  
 183 temperature in 1 s. Owing to the rapid heat exchange, the  
 184 temperature of the nanoparticles in the ascending gas current  
 185 is similar to that of the surrounding gas.

To identify the size, shape, and polymorph changes of the nanoparticles produced in the ascending gas current, we collected the nanoparticles at different heights from the evaporation source and observed them using a TEM. The floating nanoparticles were attached on SUS sheets set at 10 mm beside the evaporation source (side collector) and at  $\sim 250$  mm above the evaporation source (roof collector) (Figure S1). Nanoparticles collected at the side collector (placed at the height of the Mo wire) are mainly composed of needle-shaped particles, accompanied by a small number of cubic shaped particles (Fig. 1a). Corresponding electron diffraction (ED) patterns (Fig. 1b) and the crossing angle of the lattice fringes (obtained in high-resolution images of a needle particle; see Fig. 2) consistently matched monoclinic  $MoO_3$  with a unit cell size of  $a = 7.118$  Å,  $b = 5.366$  Å, and  $c = 5.568$  Å (JCPDS card no. 47-1081). The needle particles were always elongated along [011]. In contrast, most of the samples collected at the top of the chamber were cubic or polyhedral (Fig. 1c). Though clear distinction between cubic and polyhedral particles were difficult because some cubic particles had roundish edges and irregularly deformed outlines, the number of cubic particles was more dominant than polyhedral particles in all samples. The ED patterns of these particles were also consistent with monoclinic  $MoO_3$  (Fig. 1d). The rings corresponding to  $(11\bar{1})$  and  $(200)$  (indicated by the orange lines in Fig. 1d) do not appear in the ED pattern of the needle-shaped particles in Fig. 1b. The needle particles showed well-aligned lattice images of  $(011)$ , but frequent defects in the perpendicular planes.

The lengths of the long and perpendicular (short) axes were measured in samples collected at various heights above the evaporation source (Fig. 3a). The short axis was measured along the middle part of the nanoparticles. The average lengths of the axes (long axis, short axis), measured from at least 126 particles in each sample, were  $(24.3 \pm 2.5, 9.9 \pm 0.7)$ ,

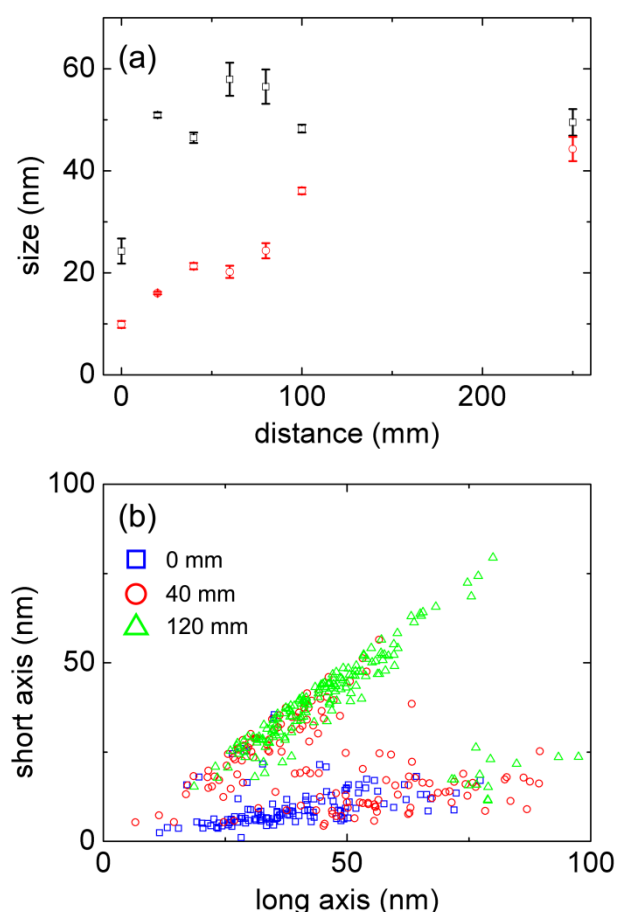


Figure 3. (a) Averaged lengths of the long axis (black squares) and short axis (red squares) of the nanoparticles collected at 0, 20, 40, 60, 80, 120 and ~250 mm above the evaporation source, plotted with their error bars, and (b) the size distributions of samples collected at 0 mm (blue squares), 40 mm (red squares) and 120 mm (green squares).

220 (50.9 ± 0.5, 16.0 ± 0.3), (46.5 ± 1.0, 21.3 ± 0.6), (58.0 ± 3.4, 20.2  
 221 ± 1.5), (56.5 ± 3.4, 24.4 ± 1.5), (48.3 ± 0.8, 36.1 ± 0.7), and  
 222 (49.5 ± 2.6, 44.3 ± 2.4) nm at collection heights of 0, 20, 40, 60  
 223 80, 120, and ~250 mm, respectively. The longitudinal length of  
 224 the nanoparticles increased from 0 to 20 mm and thereafter  
 225 remained nearly constant. In contrast, the short axis increased  
 226 continuously as the height increased from 0 mm to 250 mm.  
 227 We show the representative long/short axis ratio of the  
 228 particles collected at 0, 40 and 120 mm on the side collector in  
 229 Figure 3b. The ratio of the particles of all sample were  
 230 summarized in Figure S4. The size evolves because the number  
 231 of cubic and polyhedral particles increases while the number  
 232 of needle particles diminishes. Therefore, we measured the IR  
 233 absorbance of the floating nanoparticles in the gas current  
 234 around the evaporation source at different heights, and  
 235 compared the spectra with the ex-situ IR spectra of the  
 236 collected particles.

237 To demonstrate the evolution of the IR spectra of the  
 238 nucleated molybdenum oxide nanoparticles, we conducted  
 239 two experimental runs (A and B) under the same conditions. In  
 240 Experiment A, we surveyed from 10 mm below to 10 mm  
 241 above the evaporation source (Figure 4A1-5). In Experiment B

42 we scanned the growth of nanoparticles in the smoke from 7.5  
 43 mm to 67.5 mm above the evaporation source (Figure 4B1-13).  
 44 Once the temperature of the evaporation source had stabilized,  
 45 the scan was started in the upward direction. When the scan  
 46 reached the top in each experiment, it was returned to the  
 47 starting position and proceeded downward. Figure 4 shows  
 48 the spectra measured in the downward direction. At any given  
 49 distance from the evaporation source, the same spectral  
 50 features were observed in the upward direction (Figure S5).  
 51 The IR evolution shows a clear spatial dependence. The spectra  
 52 measured at 10 mm above the evaporation source in  
 53 Experiment A (Figure 4A5) were identical to those measured at  
 54 7.5 mm above the evaporation source in Experiment B (Figure  
 55 4B1). The shape of the IR absorption band continuously  
 56 changed from 10 mm beneath the evaporation source to 67.5  
 57 mm above the evaporation source. The swell in the 1000–750  
 58 cm<sup>-1</sup> region is contributed by at least six subtle absorptions  
 59 (indicated by the blue lines in Figure 4). The combination of  
 60 these subtle absorptions alters the shape of the IR spectra in  
 61 that region from singly to doubly peaked.

62 The spectral features were compared with those obtained by  
 63 ex-situ IR measurements of nanoparticles collected at the  
 64 same height and embedded into KBr pellets (Figure 4K1, K2;  
 65 Figure S6). In the ex-situ IR spectrum of the needle particles  
 66 collected on the side collector at 0 mm, the strongest  
 67 absorption appears at 860 cm<sup>-1</sup>. A single swell in the 1000–750  
 68 cm<sup>-1</sup> region also appears. In contrast, the ex-situ IR spectrum  
 69 of the cubic nanoparticles collected at ~250 mm exhibits peaks  
 70 at 880 and 780 cm<sup>-1</sup>, and a double-swell in the 1000–750 cm<sup>-1</sup>  
 71 region. With increasing collection height, the in-situ IR spectra  
 72 undergo a transition from the single- to double-swell  
 73 absorptions, consistent with the ex-situ IR measurements.  
 74 Note that the IR spectral features are influenced by  
 75 electromagnetic interactions between the particles and the  
 76 embedding KBr medium.<sup>30</sup> Therefore, the peak positions are  
 77 shifted toward lower wavenumbers, and the band widths are  
 78 larger, than in IR spectra measured in the free-flying state.  
 79 Despite these differences, the whole profile of the absorption,  
 80 including the single and double swells, reflects the shape of  
 81 MoO<sub>3</sub> nanoparticles. We conclude that the collected particles  
 82 were frozen and their characteristics were negligibly changed  
 83 after deposition on the side and top collectors.

84 The whole profile of the IR spectra is dominated by the  
 85 superposition of sub-peaks at 1000–750 cm<sup>-1</sup>, which have  
 86 been suggested to arise from Mo–O stretching vibrations.<sup>29</sup>  
 87 The relative intensities of the sub-peaks depend on the  
 88 crystallographic anisotropy of the nanoparticles. The in-situ FT-  
 89 IR measurements of the just-nucleated nanoparticles show  
 90 peak in the 1000–750 cm<sup>-1</sup> region, with the strongest  
 91 absorption at 840 cm<sup>-1</sup> (Figure 4). As the nanoparticles cool in  
 92 the ascending gas current, the peaks at 900 and 910 cm<sup>-1</sup> are  
 93 gradually enlarged, whereas the peaks at 970 and 860 cm<sup>-1</sup> in  
 94 spectrum A1 are reduced in spectrum B13. The characteristic  
 95 absorptions at 970 and 860 cm<sup>-1</sup> of the just-nucleated  
 96 nanoparticles are attributable to needle particles, and the  
 97 relatively strong absorptions at 920, 910, 900 and 840 cm<sup>-1</sup> are  
 98 attributable to cubic and/or polyhedral particles.

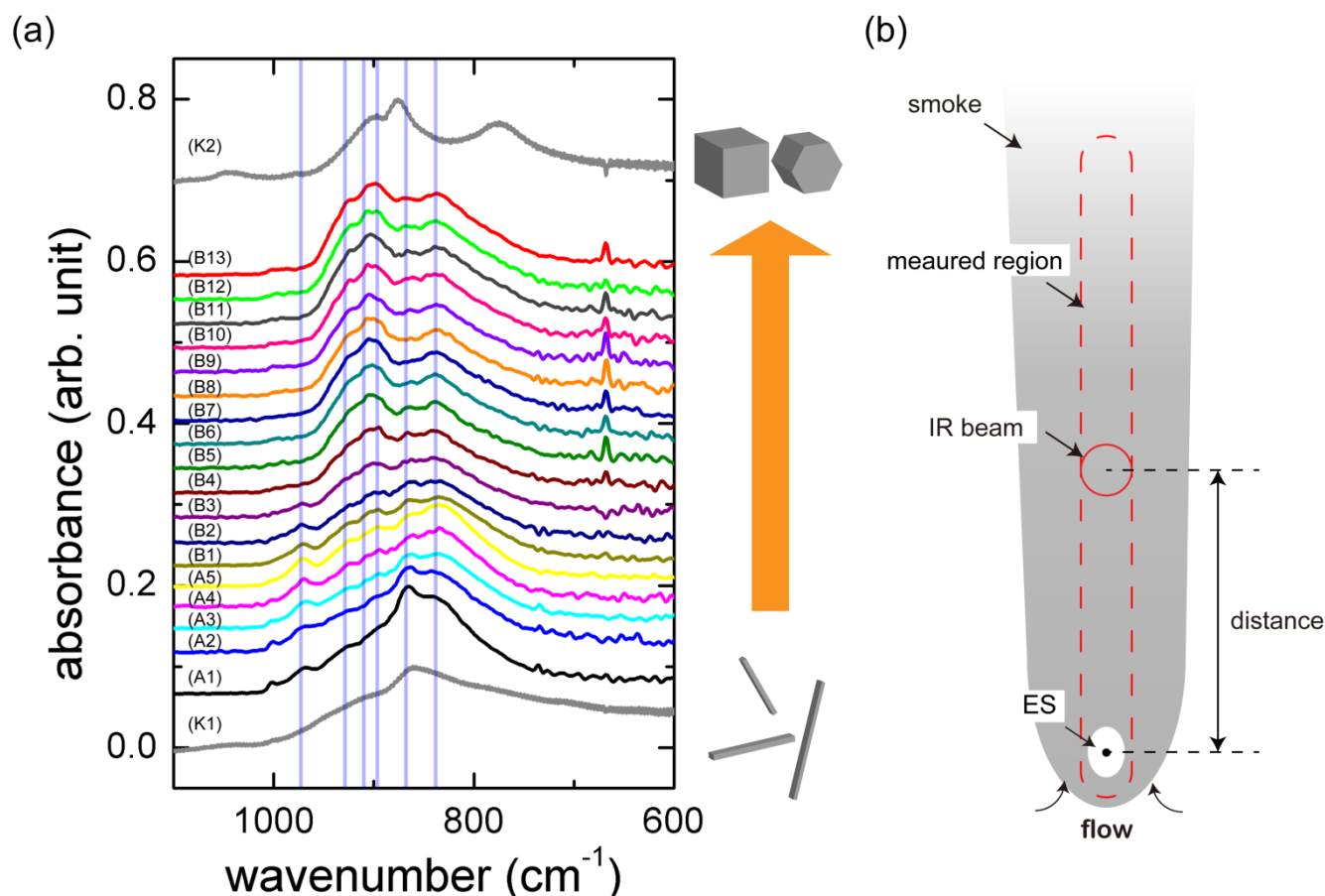


Figure 4. In-situ FT-IR spectra of nucleating and growing nanoparticles in a gas current (a) and a schematic view of the experiment along the evaporation source (ES) (b). In Experiment A, spectra were measured at 10 mm (A1) and 5 mm (A2) beneath the evaporation source, and at 0 mm (A3), 5 mm (A4), and 10 mm (A5) above the evaporation source. In Experiment B, they were measured at 7.5 (B1), 12.5 (B2), 17.5 (B3), 22.5 (B4), 27.5 (B5), 32.5 (B6), 37.5 (B7), 42.5 (B8), 47.5 (B9), 52.5 (B10), 57.5 (B11), 62.5 (B12) and 67.5 mm (B13) above the evaporation source. All spectra were obtained in the downward direction. Blue lines indicate the peaks at 970, 920, 910, 900, 860 and 840  $\text{cm}^{-1}$ . The spectra labeled K1 and K2 are the IR spectra of the needle particles and the cubic/polyhedral particles, respectively, measured by the KBr embedding method.

## 299 Discussions

300 We have questioned how the needle particles transform into  
 301 cubic and polyhedral particles in the ascending gas current.  
 302 In our experimental set up, the evaporant flowed by convection  
 303 and is quenched at temperature gradients  $>1000 \text{ K s}^{-1}$ . The  
 304 observed characteristic features of the just-nucleated  
 305 nanoparticles were attributed to the needle-shaped  
 306 molybdenum oxide (spectrum A1 in Figure 4). In previous  
 307 studies, we determined the partial pressure of the source  
 308 molecules at the nucleation point as  $\sim 10^3 \text{ Pa}$ .<sup>19–21</sup> In such an  
 309 atmosphere, a nanoparticle grows to several tens of  
 310 nanometers in  $10^{-3} \text{ s}$ ,<sup>19,20</sup> with simultaneous consumption of  
 311 the vaporized source molecules. The time scale of vapor  
 312 growth is several orders of magnitude faster than the time  
 313 scale of convection ( $\sim 1 \text{ s}$  from the evaporation source to the  
 314 top of the chamber, estimated from the convection of visible  
 315 smoke). In addition, the  $\text{MoO}_3$  vapor pressure at more than 5  
 316 mm above the evaporation source, estimated from  
 317 temperature fields derived from thermocouple data (Figure  
 318 S7), is  $<10^{-6} \text{ Pa}$ . Thus, the vapor growth by molecular  
 319 consumption should finish immediately after nucleation, which

320 initiates within several millimeters of the evaporation source.  
 321 The nanoparticles are needle-shaped by anisotropic vapor  
 322 growth. In our previous experiments, nucleation of the non-  
 323 crystalline precursor was revealed in the IR spectra of  $\text{Al}_2\text{O}_3$   
 324 and  $\text{TiO}_2$ .<sup>28,31</sup> As the IR spectrum of the just-nucleated  
 325 nanoparticles already reveals monoclinic crystal formation and  
 326 differs from that of non-crystalline particles, the phase  
 327 transition from non-crystalline to crystalline form may occur  
 328 earlier than the time scale of vapor growth. However, direct  
 329 nucleation of crystalline particles from the evaporated vapor  
 330 cannot be excluded from the possible formation pathway.  
 331 In-situ measurement revealed that the needle nanocrystals  
 332 evolved into cubic and polyhedral nanocrystals at more than  
 333 10 mm above the evaporation source. In addition, the IR  
 334 spectral features of the collected nanoparticles transitioned from  
 335 single- to double-swell, even in the 50–250 mm region. The  
 336 temperature variation at increasing vertical distance from the  
 337 evaporation source (which was maintained at  $1900 \pm 100 \text{ K}$ )  
 338 was measured by a K-type thermocouple (Figure S7). The gas  
 339 temperature of the growing region was below 673 K,<sup>32</sup> and the  
 340 vapor pressure of  $\text{MoO}_3$  was below  $10^{-6} \text{ Pa}$ . The size evolution  
 341 along the short axis of the collected nanoparticles also  
 342 revealed that growth proceeded under extremely low vapor

343 pressure conditions. This strongly suggests that the growth  
 344 and transformation are induced by coalescence, because no  
 345 growth units remained in the vapor at such low temperatures.  
 346 According to the size distributions of the particles collected at  
 347 different heights, the number of needle particles decreased at  
 348 higher collection points, while the number of cubic/polyhedral  
 349 particles increased. This indicates an evolution from smaller to  
 350 larger particles with increasing distance from the evaporation  
 351 source (Figure 3b and Figure S4). Here particles with  
 352 short/long axis ratios above 0.8 and below 0.4 were defined as  
 353 cubic/polyhedral and needle-shaped, respectively. Cubic or  
 354 polyhedral particles with a relatively larger long axis than that  
 355 of needle particles were not observed. In addition, the number  
 356 of smaller cubic/polyhedral particles did not decline,  
 357 suggesting negligible growth by monomer attachment. All of  
 358 these results are consistent with the coalescence of needle  
 359 particles into cubic and polyhedral nanocrystals.

360 To compare the attachment number of the needle particles  
 361 required to construct a cubic crystal (~10 particles) with the  
 362 collision number in the free-flying state, we then estimated  
 363 the collision frequency between the needle particles in a  
 364 simple simulation, ignoring the decreased number density of  
 365 the needle crystals during coalescence. The partial pressure of  
 366  $\text{MoO}_3$  was set to its typical value at the nucleation point (400  
 367 Pa). At this pressure, the needle particles were sized at 50.9  
 368 nm  $\times$  16.0 nm and their number density was  $3.5 \times 10^{20}$  m<sup>-3</sup>.  
 369 This suggests that the particles are free-flying over a (300  $\times$  300)  
 370 nm<sup>2</sup> area. We carried out a simple 2D random walk  
 371 simulation (see Supplementary Information). The simulated  
 372 collision frequency between the needle particles was  $10^6$   
 373 s<sup>-1</sup>, implying that the number of collisions between the needle  
 374 particles is several orders of magnitude larger than the  
 375 number of attachments required to grow a cubic nanocrystal  
 376 from the needle particles. This implies that the needle particles  
 377 incorporate into the crystal only when their approach direction  
 378 aligns with the crystallographically equivalent planes. This  
 379 approach minimizes the total free energy of the resulting  
 380 particle, suggesting that newly approaching needle particles  
 381 preferentially incorporate into a kink site, as occurs in typical  
 382 crystals.

383 Needle particles were never randomly attached  
 384 aggregated, nor elongated perpendicularly to the [011]  
 385 direction, over the cubic shape. Despite the most of  
 386 resulting particles are transformed to cubic or polyhedral  
 387 shape, the number of the particles with the intermediate  
 388 short/long axis ratio (0.4-0.8) were relatively small in all  
 389 samples (Figure S4). Attachment probability of an intermediate  
 390 particle composed of several needle particles may be higher  
 391 than that of single needle particle because the intermediate  
 392 particle should have kink sites, or a few nanometer steps  
 393 between attached needle particles due to inhomogeneity of  
 394 the size of monomers (needle particles).

395 Aggregates of multiple needle particles with the same  
 396 crystallographic orientation were frequently observed in  
 397 samples collected at 20–80 mm above the evaporation source  
 398 (Figure S8). The ED patterns of single needle particles (Fig. S9)  
 399 are streaked in the [200] direction, evidencing that stacking

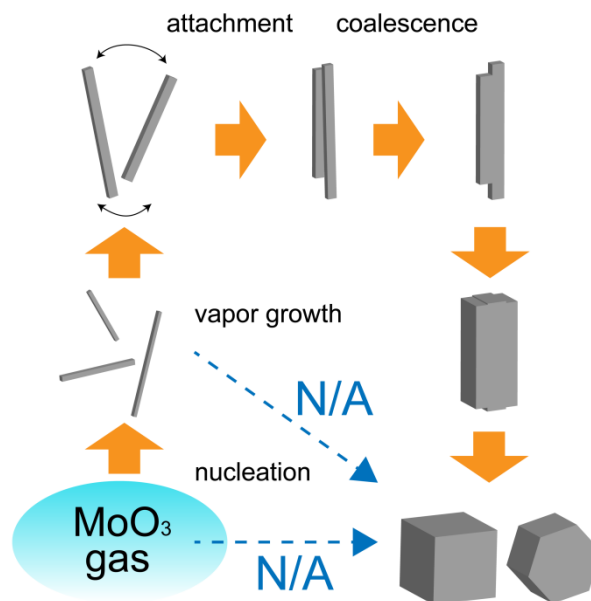


Figure 5. Schematic showing the shape evolution of just-nucleated  $\text{MoO}_3$  nanoparticles in an ascending gas current. Previously considered mechanisms shown by dotted arrows (direct nucleation or monomer-by-monomer growth in vapor) are not applicable to the formation of cubic and polyhedral  $\text{MoO}_3$  particles.

400 faults formed on (100). Owing to the attachments of the  
 401 needle particles, these stacking faults were periodic. Increased  
 402 structural defects caused by imperfect alignment during  
 403 oriented attachment has been reported in previous  
 404 studies.<sup>23,25</sup> Therefore, cubic and polyhedral particles probably  
 405 form by coalescence between the needle particles in planes  
 406 perpendicular to [011] in the ascending gas current.

407 The role of coalescence during frequent collisions in the  
 408 smoke of just-nucleated nanoparticles has been already  
 409 reported in the size evolution of metal and metal-oxide  
 410 nanoparticles. These collisions are thought to form connected  
 411 nanoparticles at surfaces, indicating that the molecules at the  
 412 surface of just-nucleated nanoparticles has significant  
 413 mobility.<sup>32–34</sup> The surface molecular diffusion may form the  
 414 faceted shapes. Attachment in crystallographically favorable  
 415 orientations was previously recognized in limited temperature  
 416 regions, but was never thought to majorly affect the  
 417 morphology of nanoparticles. At the bulk surface of  $\text{SnO}_2$ ,  
 418 nanorods rotate to fit an equivalent plane before inserting into  
 419 that plane, even in vacuum.<sup>35</sup> Such coalescence induced by  
 420 grain rotation is widely recognized.<sup>36</sup> We conclude that  
 421 selective coalescence at the crystallographically equivalent  
 422 planes of the just-nucleated nanoparticles, namely, oriented  
 423 attachment, strongly influenced the resulting morphology in  
 424 our experiments. The formation sequence of cubic and  
 425 polyhedral  $\text{MoO}_3$  particles in vapor is schematically illustrated  
 426 in Figure 5.

427 Oriented attachment growth is suggested to proceed by  
 428 three driving forces; a thermodynamic driving force that  
 429 reduces the energetic disadvantage at the surface, Coulombic  
 430 (electrostatic) interactions, and van der Waals interactions.  
 431 Competition between these forces, which depend on the  
 432 orientation and surrounding medium, obscures the driving  
 433 force of coalescence growth.<sup>26</sup> If the main driving force arises

434 from thermodynamic requirement, a particle collides at the  
 435 edge of another particle should be incorporated to reduce the  
 436 energetic disadvantage at free surface. None of the needle  
 437 particles aggregated in random orientations or in inequivalent  
 438 planes suggests collision among particles always occurs at the  
 439 central part of another particle. In contrast, Coulombic force  
 440 interacts between particles and may attract each other at the  
 441 central part, leading attachment at the near center. In aqueous  
 442 solution, Coulombic interactions between particles decay  
 443 exponentially with distance, as they are mediated by the ionic  
 444 screening effect. Elimination of interfacial solvent molecules  
 445 also influences the growth process. In addition, the surface  
 446 energy differences between the planes are reduced in aqueous  
 447 solution. In some simulation studies, the coalescence  
 448 mechanisms of nanoparticles clearly differed in vacuum and  
 449 solution.<sup>26,27</sup> Comparisons between these processes might  
 450 elucidate the driving force of oriented attachment. In our  
 451 experiments, large differences of surface energy between the  
 452 fresh planes of the just-nucleated nanoparticles were expected,  
 453 and the Coulombic forces should extend over much larger  
 454 distances than in aqueous solution.

455 We present the first experimental report on the oriented  
 456 attachment of free-flying nanoparticles in vapor. Such self-  
 457 assembly growth in vapor is potentially applicable to industrial  
 458 synthesis processes, and might explain natural mineral  
 459 evolution such as cosmic dust aggregation during planet  
 460 formation.<sup>37</sup> In the present experimental setup, we cannot  
 461 distinguish between free-flying particles that have attached  
 462 after electrostatic alignment and particles that have randomly  
 463 attached, then immediately aligned to reduce the misfit.  
 464 In the previous consensus view, homogeneous nucleation  
 465 from vapor occurs by a direct monomer-by-monomer process  
 466 from molecules to crystals. However, our previous works  
 467 revealed that metal-oxide nanoparticles crystallize by  
 468 multistep processes.<sup>28,31,38</sup> The present study reveals a growth  
 469 pathway of nanoparticles via oriented attachment, which has  
 470 never been considered in nucleation and subsequent growth  
 471 processes in vapor. These findings suggest that the versatile  
 472 nucleation and growth pathways demonstrated in solution  
 473 systems throughout the past decade also occur in vapor  
 474 systems.

## 475 Conclusions

476 We measured the IR spectra during the formation of final  
 477 crystals from homogeneously distributed just-nucleated Meq  
 478 crystals in a highly supersaturated vapor. The crystals grew by  
 479 oriented attachment. In the first step, needle particles form  
 480 anisotropic vapor growth around the evaporation source. The  
 481 size of the critical nucleus was estimated as fewer than tens of  
 482 molecules. The nuclei grew rapidly, forming 10-nm-scale  
 483 needles in 0.1 s while rapidly exhausting the source gas. The  
 484 free-flying needle particles collided in approximately 1 s.  
 485 Finally, the needle particles attached in crystallographically  
 486 equivalent planes, forming cubic and polyhedral nanoparticles.  
 487 Attachment in crystallographically favorable orientations  
 488 which has not been previously recognized in nanoparticle  
 489 formation in vapor, critically determines the properties of the

resulting particles and is comparable to the typical growth  
 process of macromolecular crystals. In this case, the growth  
 units are the needle particles. This result provides new insights  
 into the control of chemical compositions, morphologies, and  
 polymorphs of industrial nanomaterials, and assists our  
 understanding of cosmic dust aggregation in early solar  
 systems.

## Acknowledgements

We thank F. Saito, S. Nakatsubo, S. Mori, and K. Shinbori of  
 the Technical Division in the Institute of Low Temperature  
 Science, Hokkaido University, for their help in the  
 development of the experimental system. This work was partly  
 supported by a Grant-in-Aid for a JSPS Fellow (15J02433) and a  
 Grant-in-Aid for Scientific Research(S) from KAKENHI  
 (15H05731).

## Notes and references

- 1 S.-Y. Chung, Y.-M. Kim, J.-G. Kim and Y.-J. Kim, *Nat. Phys.*, 2009, **5**, 68–73.
- 2 A. E. S. Van Driessche, L. G. Benning, J. D. Rodriguez-Blanco, M. Ossorio, P. Bots and J. M. Garcia-Ruiz, *Science*, 2012, **336**, 69–72.
- 3 M. H. Nielsen, S. Aloni and J. J. De Yoreo, *Science*, 2013, **218**, 213–218.
- 4 D. C. Gary, M. W. Terban, S. J. L. Billinge and B. M. Cossairt, *Chem. Mater.*, 2015, **27**, 1432–1441.
- 5 J. Baumgartner, A. Dey, P. H. H. Bomans, C. Le Coadou, P. Fratzl, N. A. J. M. Sommerdijk and D. Faivre, *Nat. Mater.*, 2013, **12**, 310–314.
- 6 D. Loh, S. Sen, M. Bosman, S. F. Tan, J. Zhong, C. A. Nijhuis, P. Kral, P. Matsudaira and U. Mirsaidov, *Nat. Chem.*, 2016, 1–10.
- 7 M. K. Bera and M. R. Antonio, *J. Am. Chem. Soc.*, 2016, **138**, 7282–7288.
- 8 C. J. S. Ibsen, D. Gebauer and H. Birkedal, *Chem. Mater.*, 2016, **28**, 8550–8555.
- 9 S. Parveen, R. J. Davey, G. Dent and R. G. Pritchard, *Chem. Commun. (Camb.)*, 2005, 1531–1533.
- 10 K. Harano, T. Homma, Y. Niimi, M. Koshino, K. Suenaga, L. Leibler and E. Nakamura, *Nat. Mater.*, 2012, **11**, 877–881.
- 11 C. Sun and D. Xue, *Cryst. Growth Des.*, 2015, **15**, 2867–2873.
- 12 P. G. Vekilov, *Nanoscale*, 2010, **2**, 2346–2357.
- 13 T. Yamazaki, Y. Kimura, P. G. Vekilov, E. Furukawa, M. Shirai, H. Matsumoto, A. E. S. Van Driessche and K. Tsukamoto, *Proc. Natl. Acad. Sci.*, 2017, **114**, 201606948.
- 14 T. H. Zhang and X. Y. Liu, *J. Phys. Chem. B*, 2007, **111**, 14001–14005.
- 15 J. R. Savage and A. D. Dinsmore, *Phys. Rev. Lett.*, 2009, **102**, 15–18.
- 16 W. Ostwald, *Zeitschrift für Phys. Chemie*, 1897, **22**, 289–302.

- 541 17 D. Chakraborty and G. N. Patey, *J. Phys. Chem. Lett.*, 2013,  
542 **4**, 573–578.
- 543 18 J. Ihli, W. C. Wong, E. H. Noel, Y.-Y. Kim, A. N. Kulak, H. K.  
544 Christenson, M. J. Duer and F. C. Meldrum, *Nat. Commun.*,  
545 2014, **5**, 3169.
- 546 19 Y. Kimura, H. Miura, K. Tsukamoto, C. Li and T. Maki, *J.*  
547 *Cryst. Growth*, 2011, **316**, 196–200.
- 548 20 Y. Kimura, K. K. Tanaka, H. Miura and K. Tsukamoto, *Cryst.*  
549 *Growth Des.*, 2012, **12**, 3278–3284.
- 550 21 Y. Kimura, K. K. Tanaka, T. Nozawa, S. Takeuchi and Y.  
551 Inatomi, *Sci. Adv.*, 2017, **3**, e1601992.
- 552 22 N. T. K. Thanh, N. Maclean and S. Mahiddine, *Chem. Rev.*,  
553 2014, **114**, 7610–7630.
- 554 23 R. L. Penn and J. F. Banfield, *Science*, 1998, **281**, 969–971.
- 555 24 J. F. Banfield, *Science*, 2000, **289**, 751–754.
- 556 25 D. Li, M. H. Nielsen, J. R. I. Lee, C. Frandsen, J. F. Banfield  
557 and J. J. De Yoreo, *Science*, 2012, **336**, 1014–1018.
- 558 26 H. Zhang and J. F. Banfield, *CrystEngComm*, 2014, **16**,  
559 1568–1578.
- 560 27 M. Raju, A. C. T. Van Duin and K. A. Fichthorn, *Nano Lett.*,  
561 2014, **14**, 1836–1842.
- 562 28 S. Ishizuka, Y. Kimura, T. Yamazaki, T. Hama, N. Watanabe  
563 and A. Kouchi, *Chem. Mater.*, 2016, **28**, 8732–8741.
- 564 29 M. Kurumada and C. Kaito, *J. Phys. Soc. Japan*, 2006, **75**, 2–  
565 6.
- 566 30 C. F. Bohren and D. R. Huffman, *Absorption and Scattering*  
567 *of Light by Small Particles*, John Wiley & Sons., New York,  
568 United States, 1983.
- 569 31 S. Ishizuka, Y. Kimura and T. Yamazaki, *J. Cryst. Growth*,  
570 2016, **450**, 168–173.
- 571 32 C. Kaito, *Jpn. J. Appl. Phys.*, 1978, **17**, 601–609.
- 572 33 C. Kaito, *Jpn. J. Appl. Phys.*, 1985, **24**, 261–264.
- 573 34 O. Kido, H. Suzuki, Y. Saito and C. Kaito, *Jpn. J. Appl. Phys.*,  
574 2003, **42**, 5705–5708.
- 575 35 C. Ribeiro, E. J. H. Lee, T. R. Giraldo, R. Aguiar, E. Longo and  
576 E. R. Leite, *J. Appl. Phys.*, 2005, **97**, 24313.
- 577 36 D. Moldovan, V. Yamakov, D. Wolf and S. R. Phillpot, *Phys.*  
578 *Rev. Lett.*, 2002, **89**, 206101.
- 579 37 S. Okuzumi, M. Momose, S. Sirono, H. Kobayashi and H.  
580 Tanaka, *Astrophys. J.*, 2016, **821**, 82.
- 581 38 S. Ishizuka, Y. Kimura and I. Sakon, *Astrophys. J.*, 2015, **803**,  
582 88.  
583